Vertically aligned graphene prepared by photonic annealing for ultra-sensitive biosensor

Lue Wang[†‡], Wei Zhang[†‡*], Siamak Samavat[‡], Davide Deganello[‡] and Kar Seng Teng[‡*]

[‡]*College of Engineering, Swansea University, Bay Campus, Swansea SA1 8EN, UK.*

Abstract

Graphene exhibits excellent physical, electronic and chemical properties that are highly desirable for biosensing application. However, most graphene biosensors are based on graphene lying flat on a substrate and therefore not utilizing its maximum specific surface area for ultra-sensitive detection. Herein, we showcased the novel use of photonic annealing on flexographic printed graphene-ethyl cellulose composite to produce vertically aligned graphene (VAG) biosensors for ultra-sensitive detection of algal toxin in drinking water. These VAG structures, which maximized the specific surface area of graphene, were formed by partial removal of the polymeric binder upon applying the intense pulsed light on the printed graphene. A label-free and low-cost VAG biosensor based on non-faradaic electrochemical impedance spectroscopy technique was fabricated. The biosensor exhibited a limit of detection (LoD) of 1.2 ng/L for MC-LR in local tap water. Such ultra-sensitive VAG biosensor is suitable for low-cost mass production using an integrated roll-to-roll flexographic printing with rapid photonic annealing technique.

Keywords: Graphene; Flexographic printing; Photonic annealing; Biosensor; Algal toxins; Non-faradaic EIS

Recent advances in graphene related nanomaterials have led to major technological advancement in solar energy harvesting and storage[1], water desalination[2, 3] and electronics[4] etc. Its superiority in electrical conductivity, theoretical surface area[5], biocompatibility and multifunctionality[6] are envisaged to provide extraordinary performance and affordable solutions for next-generation biosensing platforms.[7, 8, 9, 10, 11] Indeed, there has been significant research interests in developing graphene-based biosensors that can provide ultra-sensitive and early alert detection. To date, most of these biosensors were reported with graphene lying flat on an electrode substrate. Such configuration does not fully utilise the surface area of graphene for biosensing applications. To maximise its surface area, graphene has been shown to be grown vertically on a substrate via chemical vapour deposition (CVD).[12,13] However, the growth technique is costly, time-consuming and requires complex processing steps. Therefore, it is of great interests to develop ultra-sensitive vertically aligned graphene (VAG) biosensor that is feasible for cost-effective mass production to bring the technology to mass market.

Roll to roll flexographic printing is a high throughput technique that allows high speed selective patterning and direct deposition of materials (via ink formulations) without the use of expensive photolithography and high vacuum equipment.[14,15] Previously, the authors flexographically printed electrochemical enzymatic and impedimetric biosensors based on ZnO nanowires[16] and nanotextured surface of ZnO thin film[17]on organic substrates, respectively. The use of organic substrates with the printing technique would significantly reduce the product cost. Flexographic printing of graphene nanoplatelets and carbon nanotubes have also been performed for application in dye sensitised solar cell[18] and resistive heater[19], respectively.

In this work, flexographic printing was used to produce graphene interdigitated electrodes using ink comprised of ball-milled graphene nanoplatelets (GNPs) and ethyl cellulose (EC). The latter was used as binder as well as dispersion stabiliser in the graphene ink. The printed electrodes were then photonic annealed, which resulted in dense VAG at the electrodes after partial removal of EC. The annealing technique uses intense pulsed light to provide rapid (e.g. milliseconds) localised heating due to optical absorption at the deposited film, while limiting thermal damage to the substrate. It has gained much attention recently, for example, Paglia *et al* employed photonic annealing to reduce inkjet-printed CuO nanocrystals on polyethylene terephthalate (PET) substrate into sintered copper film.[20] Arapov *et al* observed that photonic annealing can enhance the conductivity of polymeric binder containing graphene ink printed on PET substrate using stencil method.[21] The use of photonic annealing to create dense porous microstructure in graphene inks, consisting of nitrocellulose as binder, for micro-supercapacitors application was reported by Secor *et al*.[22] Das *et al* reported a rapid pulse laser annealing on inkjet-printed graphene for paper-based electronics and electrochemical devices.[23,24] To the best knowledge of the authors, photonic annealing has not been performed on flexographic printed graphene film, which produced VAG at the electrodes. These graphene-based electrodes are potentially suitable for ultra-sensitive biosensing applications due to significantly increased surface area.

Herein, we reported a cost-effective and high-volume production of novel VAG biosensor enabled by the integration of roll-to-roll flexographic printing with rapid photonic annealing technique. The VAG biosensors were based on non-faradaic electrochemical impedance spectroscopy (EIS) technique, which offered label-free, rapid and direct detection of biomarkers. Unlike faradaic EIS biosensor, it does not require redox species, and hence it is easy to operate and is well-suited for real-time monitoring. Any physical change at the biosensor due to biorecognition events, such as antigen-antibody binding, will result in the perturbation of double layer capacitance at the electrode surface leading to a phase shift between the input voltage and output current over a range of frequencies.[25,26] Functionalisation of the biosensor was performed using spray coating technique to preserve the VAG structures. Key fabrication processes of the biosensor are illustrated in Figure S1. The VAG biosensor were functionalised to detect algal toxin microcystins-LR (MC-LR), a most widely occurring variant and well-known potent hepatotoxins, in drinking water due to increasing occurrence of harmful algal bloom events around globe.[27] The algal toxins are posing enormous challenges to current water supply practice, in terms of both monitoring and treatment control.[28,29] Following a significant harmful algal bloom event, there is an urgent need to develop a cost-effective and quick turnaround monitoring technology.[30,31] In this context, the VAG biosensor in this work exhibited ultrasensitive detection of MC-LR and demonstrated excellent selectivity against other algal toxin variants and inferencing compounds.

1. Experimental

1.1 Preparation of graphene ink for flexographic printing

Graphene nanoplatelets (GNP) with diameter of 2-7 μm and thickness of 2-10 nm were purchased from Advanced Chemicals Supplier (California, USA). 1 g of GNP and 20 ml of dipropylene glycol methyl ether (DPGME) were mixed together, and then ball-milled at 300 rpm using grinding balls with diameter of 5 mm in FRITSCH Ball Miller (FRITSCH, Idar-Oberstein, Germany) for 24 h to produce GNPs with fewer graphene layers. 2 g of ethyl cellulose (EC) was mixed with 20 ml of isopropanol (IPA) with 10 min ultrasonication to form EC solution. 24 h ball milled GNP mixture was mixed with the ready-made EC solution, and then ball-milled for another 2 h to obtain a stable GNP-EC composite. HDPlas ® conductive carbon ink was purchased from HDPlas ® ink (Haydale Limited, Carmarthenshire, UK) solution was prepared by adding 41 g HDPlas ® powder in a 50/50 v/v IPA/DPGME solvent mixture.

Polyimide substrate was cleaned before printing by first dipping in IPA and then in acetone both with 10 min sonication and drying under nitrogen. Flexographic printing was carried out using RK Flexiproof 100 printer (RK Print-Coat Instruments Ltd. Hertfordshire, UK). Flexible printing plate with the design of interdigitated electrodes was taped on the flexographic plate roller while the polyimide substrate was fixed on an impression roller. The GNP ink was introduced between a doctor blade and an anilox roller (with volume of 24 cm^3/m^2), which transferred the ink to the printing plate and simultaneously printed onto the polyimide substrate. To ensure good conductivity, the substrate was firstly printed with a layer of HDPlas® as a conductive base, followed by the printing of sensing layer of GNP over the top. Between each printing cycle, the printed layer was blown dried using a hair dryer. Interdigitated electrodes featuring an array of eight fingers (e.g. each finger has a length of 5.5 mm width of 1 mm and a separation of 1 mm between each other) with a total working electrode area of 2.25 mm^2 were printed using the flexography technique.

1.2 Fabrication of VAG biosensors

The flexographic printed graphene electrodes were photonic annealed using intense pulsed light from PulseForge ® 1300 photonic curing system (NovaCentrix, Texas, USA). The optimal photonic annealing condition was a single pulse with radiant power of 3.3 kW/cm^2. Under this condition, EC was partially removed with maximum density of VAG structure. Photonic annealed VAG surface was treated with oxygen plasma for 10 min (Henniker HPT-100, flowrate 20 s.c.c.m.), which was followed by incubation in water vapour for 1 h. Functionalization of the biosensor was performed using IWATA Eclipse HP-CS Airbrush (IWATA Eclipse, Japan). The spray coating conditions were optimized (e.g. spraying distance and compressed air pressure) to preserve the VAG structures, of which the results are shown in Figure S4.

The following VAG biosensor preparation procedure is illustrated in Figure 1. After spray coating (3-Aminopropyl)triethoxysilane (APTES) , the electrodes were annealed in nitrogen at 120 °C for 20 min. Previously, annealing process has shown to densify the APTES layer, which would provide the essential blocking properties.[32] A sensing area of 5 mm × 8 mm was marked by paraffin wax over the interdigitated area. 125 μL of 5 % glutaraldehyde prepared in phosphate buffered saline (PBS) solution was sprayed on to the sensing area. PBS solution of 10 mM at pH 7.4±0.1 were purchased from Fisher Scientific (Loughborough, UK). The same area was then spray coated with 100 μL MC-LR antibodies (20 μg/mL in PBS solution). As a result, two separate aldehyde groups of the glutaraldehyde on each end of carbon chains would form covalent bond with the amine groups exposed on the APTES layer and those of MC-LR antibody (mouse IgG1, Alexi Biochemicals Inc), respectively. This was followed by spray coating with 125 μL ethanolamine (5 mM) to the same area, which is to neutralize any aldehyde groups from the unreacted glutaraldehyde. Basic solution (pH 9.5) addition would also assist the removal of loosened antibodies on the VAG biosensor surface.[33]

1.3 Characterizations

Morphology of the printed graphene electrodes was investigated by a Hitachi S-4800 scanning electron microscope (SEM). An integrated energy dispersive x-ray (EDX) spectroscopy was applied to investigate the presence of APTES on the VAG surface via element mapping of silicon. A FEI TALOS

F200X field emission gun transmission electron microscope (FEG-TEM) was employed to study the lattice structure of ball-milled GNP. The structure and defect of VAG were studied using inVia™ confocal Raman microscope (Renishaw). Surface functional groups at the VAG electrodes after plasma and water vapor treatments were investigated using Fourier transform infrared spectroscopy (FTIR, Perkin Elmer Spectrum 100) and X-ray photoelectron spectroscopy (XPS, Kratos Axis Supra) performed at room temperature. Surface roughness and topography of VAG biosensors were probed using white light interferometry (Veeco Wyko NT9300). Cyclic voltammetry (CV) and non-faradaic electrochemical impedance spectroscopy (EIS) were carried out on a Gamry Reference 600+ potentiostat.

1.4 Non-faradaic EIS biosensing of MC-LR in water

Firstly, the phase of EIS measurement was carried out on a 100 µL of PBS and used as a baseline. The pure PBS was then replaced with 100 µL of PBS spiked with MC-LR (Enzo Life Sciences), after 15 min incubation, a further EIS measurement was carried out. The change in phase between the two EIS measurements was used as non-faradaic biosensing response. The same procedure was repeated for five different concentrations ranging from 0.001 to 10 µg/L and a negative sample without any MC-LR.

To assess the specificity of detection, the VAG biosensors has undergone 15 min incubation in a mixture containing 0.1 µg/L MC-RR, MC-LR, and MC-LW, respectively. Non-faradaic EIS measurements using the same procedure were then performed on the mixture and the results were compared with biosensors tested solely on MC-LR with the same concentration of 0.1 µg/L. Local tap water samples (Swansea, UK) were also spiked with MC-LR at the same concentration to validate the biosensor performance on real drinking water, which contains many different metal ions and chemicals (e.g. fluoride, chlorine etc.).

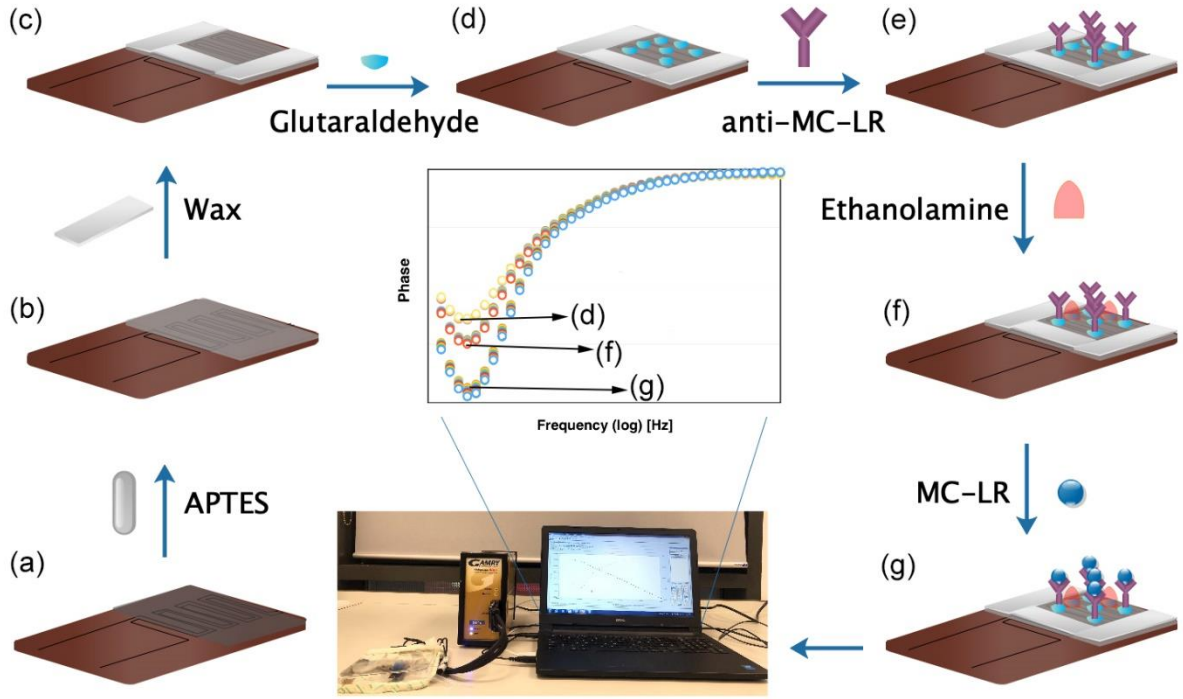

Figure 1 Surface functionalisation procedure of VAG biosensor from (a) to (g) and non-faradaic EIS measurement at the step (d), (f) and (g), respectively.

2. Results and discussion

2.1 Morphology of ball milled GNPs

GNPs were ball-milled to produce graphene sheets for the fabrication of the graphene interdigitated electrodes. Morphology of the GNPs after different durations of ball milling were studied using SEM. Figure 2(a) shows SEM image of thick and multilayered GNPs prior to ball milling, indicating the

severe agglomeration. It can also be seen that the size of GNPs was reduced drastically as the ball milling duration increased from 4 to 24 h as shown in Figure 2(b) to 2(g), respectively. A higher magnification image of GNPs after 24 h ball milling is shown in Fig. 2(h). The GNPs became much thinner with good transparency, which suggests graphene sheets having fewer layers were produced. TEM image of GNPs after 24 h ball milling is shown in Figure 2(i). It showed mono-/bi-layer thick graphene, which was almost transparent under the electron beam and consisted of wrinkles, creases, and overlapping sheets. Figure 2(j) and 2(k) show selected area electron diffraction (SAED) patterns acquired from location 'j' and 'k' in Figure 2(i), respectively. A distinctive hexagonal diffraction pattern shown in Figure 2(j) was associated with single or bi-layered graphene sheets. On the other hand, the multiple rotationally misaligned hexagonal patterns were observed in Figure 2(k), indicating that some areas were still multilayer thick especially around the edges.[34] The 24 h ball-milled GNPs were used in the formulation of graphene ink suitable for flexographic printing of interdigitated electrodes.

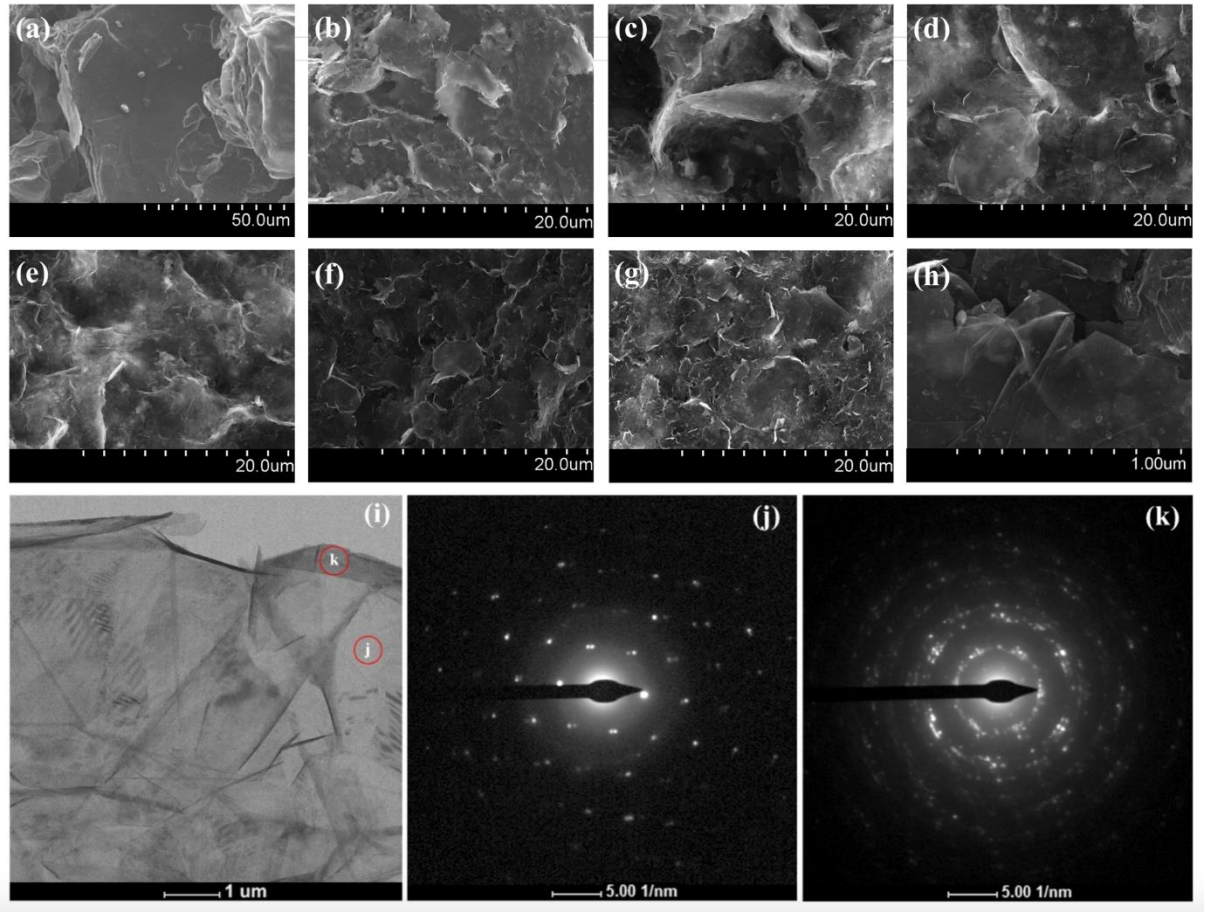

Figure 2. SEM images of GNPs after different durations of ball milling: (a) without ball milling, (b) after 4 h, (c) 8 h, (d) 12 h, (e) 16 h, (f) 20 h, (g) 24 h ball milling (2.5k magnification), and (h) higher magnification (i.e. 50k) SEM image of 24 h ball milling. (I) TEM image of 24 h ball milled GNP for flexographic printing. (J) and (K) SAED patterns from regions marked accordingly in (I).

2.2 VAG characterization on photonic annealed graphene electrodes

Photonic annealing was performed on the flexographic printed graphene electrodes and the morphology of the electrodes was studied at different radiant power density. Cross-sectional and titled SEM images of the graphene electrodes after photonic annealing are shown in Figure 3(a)–(h). When the power density was increased to 2.5 kW/cm^2, VAG began to appear at the electrode in Figure 3(e) and (f). Density of VAG structure reached maximum at 3.3 kW/cm^2 (shown in Figure 3g and h). Beyond 3.3 kW/cm^2, the graphene started to come off from the substrate. Total delamination of the graphene layer occurred at a power density greater than 5.4 kW/cm^2. The intense pulsed light resulted in localized heating at the printed graphene electrodes leading to rapid removal of polymeric binders (e.g. EC) used in the ink and subsequent formation of VAG. The optimal radiant power density was found to be 3.3

kW/cm^2 so denser VAG would provide larger specific surface area. The effect of photonic annealing on surface topography of the printed graphene was characterized using white light interferometry as shown in Figure 3(i) and (j), respectively. It further confirmed that photonic annealing has produced a dense forest-like structure of graphene at the surface of electrodes. An average surface roughness was measured to be 1.61 ± 0.14 µm before photonic annealing and significantly increased to 15.88 ± 2.12 µm after photonic annealing due to the formation of VAG.

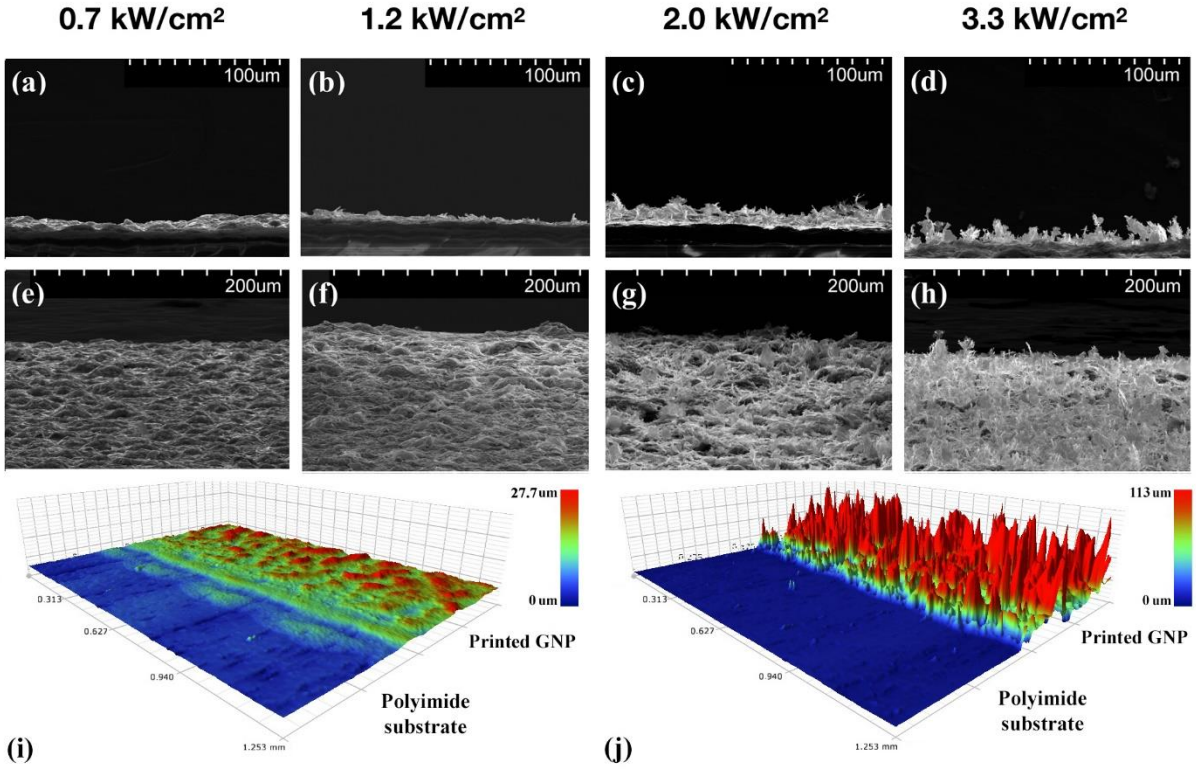

Figure 3. SEM images of VAG structures under different photonic annealing conditions: (a-d) cross-sectional and (e-h) tilted view of VAG after photonic annealed at an increased radiant power of 0.7, 1.2 , 2, and 3.3 kW/cm^2, respectively; (i) and (j) are topographical mapping using white light interferometry technique on the graphene electrode before and after photonic annealing.

2.3 Optimization of hydroxylation on the surface of VAG biosensors

Prior to functionalization of the VAG for biosensing application, its surface was first treated with oxygen plasma coupled with water vapor incubation to generate hydroxyl groups, which were required to bond with APTES and studied using Raman spectroscopy.[35] For 'control' or pristine graphene, there were two signature bands produced by the Stokes phonon energy shift in the Raman spectra: G band (1580 cm^{-1}) represented the in-plane vibration of graphene lattice and 2D band (2690 cm^{-1}) represented a second-order overtone of a different in-plane vibration in Figure 4(a) and (b).[36,37] The D (1350 cm^{-1}) and D' bands (1620 cm^{-1}) in the Raman spectra are generally related to intervalley and intravalley defect scattering, respectively. The intensity of these two bands increases when disorder or defects are introduced into graphene structure.[38] Figure 4(a) shows Raman spectra of VAG treated with different durations of oxygen plasma but with same duration of water vapor incubation, while Figure 4(b) shows VAG treated with same plasma duration but with different durations of water vapor incubation. The I_D/I_G, D and G band intensity ratio, is useful to assess the extent of defect formation in graphene after plasma treatment.[39] The I_D/I_G ratio was found in Figure 4(c) and (d) to increase sharply and then began to plateau after 10 min of plasma treatment and 1 h of water vapor incubation, which was set as optimal surface treatment conditions for VAG biosensor. The increase of I_D/I_G ratio was probably caused by hydroxyl groups generated at the surface of VAG. In typical FTIR analysis, hydroxyl groups are usually observed as a broad peak near 3500 cm^{-1} regions.[40] In this study (see Figure S2), a relatively sharp peak was apparent at ~3676 cm^{-1} and its intensity increased significantly after oxygen plasma and water vapor treatments. This further confirmed the generation of hydroxyl groups on the VAG surface,

whereas slight shifting and sharpening of the peak could due to the absence of hydrogen bonding.[41] Finally, the I_{2D}/I_G ratio of ~1.42 and full width at half-maximum (FWHM) of the 2D peaks of ~ 92 cm^{-1} indicated that optimised VAG at the electrodes consist of graphene mostly of more than five layers.[42,43] This observation was consistent with previous SAED analysis on the VAG.

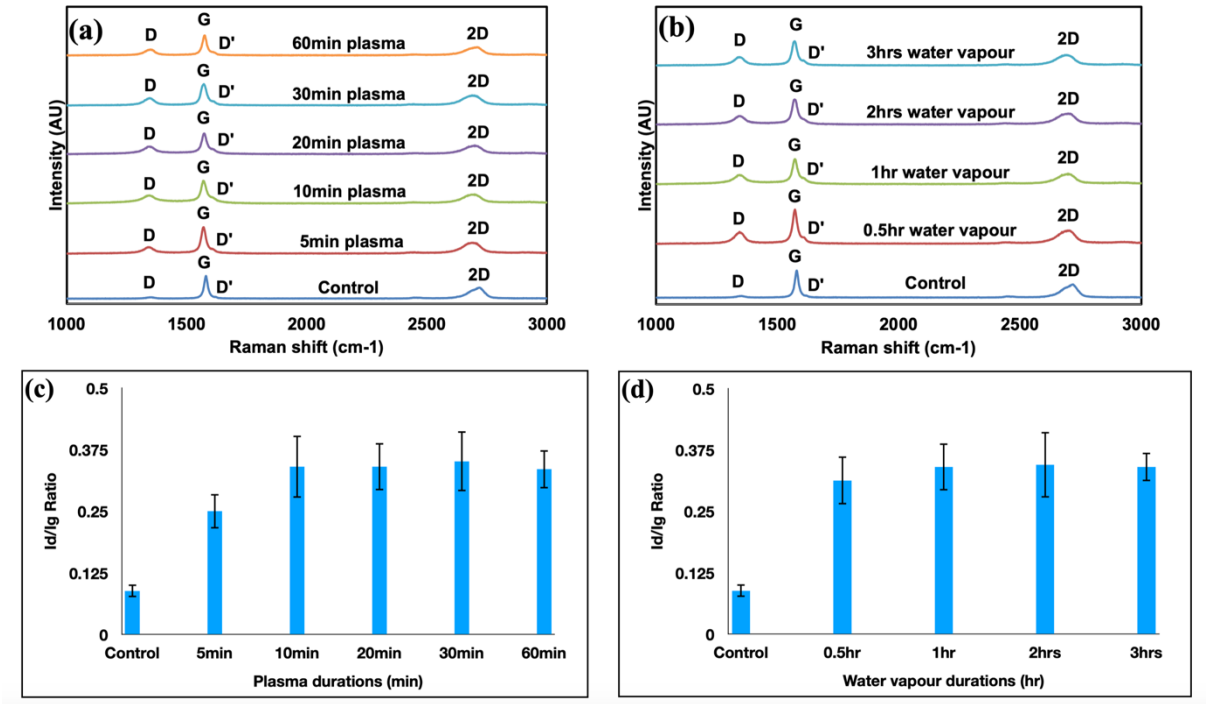

Figure 4. (a) Raman spectra of VAG after different durations of oxygen plasma treatment with 1 h water vapor incubation. (b) Raman spectra of VAG after 10 min oxygen plasma treatment with different durations of water vapor incubation. The ratios of I_D/I_G for each condition corresponding to (a) and (b) are shown in (c) and (d), respectively.

Chemical bond analysis of the VAG before and after oxygen plasma/water vapor surface treatment were carried out using XPS technique, which is shown in Figure S3(a). There were two distinctive peaks around the binding energy of 284 eV and 532 eV related to C1s and O1s, respectively. [44]**Error! Bookmark not defined.** The C1s core level before and after surface treatment, shown in Figure S3(b) and (c) respectively, was deconvoluted using two peaks. These peaks positioned at ~284 and ~285.6 eV generally belong to graphitic carbon (C-C) and carbonyl group (C=O), respectively.[45] The graphitic carbon (C-C) was attributed to the graphene, while the presence of carbonyl group (C=O) was probably due to the graphene defects. Figure S3(d) and (e) show the deconvoluted O1s core level before and after surface treatment, respectively. The peak components consisted of C-OH bond and carbonyl group (C=O) at binding energy of ~532 and ~530.9 eV, respectively.**Error! Bookmark not defined.** Ratios of each oxygen-contained functional group to graphitic carbon (C-C) were calculated by integration of corresponding peak areas. There was an increase in hydroxyl group (C-OH) to C-C ratio of almost five times from 0.11 to 0.53 after surface treatments, hence indicating that hydroxyl groups were successfully generated on the VAG surface. On the other hand, carbonyl group (C=O) to C-C ratio was found to increase barely from 0.1 to 0.14 after the same surface treatments. This suggests that the oxygen plasma generated defects were hydroxyl group dominated mostly at the edge of graphene sheet without breaking majority of σ- or π-bonds in the planar area[46], which was also consistent with Raman and FTIR analysis of the same samples.

2.4 Surface biofunctionalization and non-faradaic EIS biosensing of VAG biosensors

For non-faradaic EIS measurements, a well-formed insulating self-assembly monolayer (SAM) is essential. A well-established silanization approach was employed for chemically functionalizing hydroxylated graphene surfaces with APTES as SAM.[47] To preserve the structure of VAG, surface functionalization was performed using a spray-coating technique. Figure S5 shows EDX mapping of silicon element, which can be found in APTES, and revealed uniform distribution of APTES on the

surface of VAG after spray coating. Higher magnification cross-sectional SEM and their corresponding EDX mapping images of VAG after spray coating are shown in Figure 5(a) and (b), respectively. It was evident that VAG structures remained intact after the spray coating process, which demonstrated its suitability and reliability as an important surface functionalization technique for VAG biosensor. The effectiveness of APTES coating as an insulating SAM at the VAG was characterized electrochemically using cyclic voltammetry (CV) technique at ambient temperature. The SAM was found to block electron transfer effectively, as evidenced by CV scans shown in Figure S6, which did not exhibit any redox peak (i.e. Fe^{2+}/Fe^{3+}). This is an indicative of a well-packed SAM formation (i.e. APTES) at the surface of VAG.[48]

In a typical non-faradaic EIS process, biomolecules are bound to the electrode and displace water molecules at its surface. This alters the double layer capacitance and dielectric constant at its surface.[49] Unlike capacitance measurement, the phase change during the EIS measurement is relatively independent of the biosensing area size.[50] Therefore, phase measurement is highly desirable as it provides better reproducibility on the biosensing results against manufacturing tolerances. In theory, the phase of impedance shifts towards -90° as a result of a more insulated interface between electrode and solution, while it shifts towards zero for a non-insulated interface.[51] As shown in Figure 5(c), the observed decrease in phase towards negative after antibodies immobilization and then after binding with antigens (i.e. MC-LR) suggest an additional layer was formed at each step that further hindered the access of currents or ions to the sensor surface.

Table 1 MC-LR detection results using EIS biosensors in most recent studies.

LOD (ng/L)	Range (µg/L)	Recovery in real water samples (%)	Methods	References
-	0.05 to 100	-	Faradaic EIS	52
-	0.05 to 100	92.7	Faradaic EIS	53 **Error! Bookmark not defined.**
4	0.01 to 100	94.1-98.1	Faradaic EIS	54
2.3	0.005 to 100	93.5-98.2	Faradaic EIS	44
1.2	0.001 to 10	98.4±3.9	Non-faradaic EIS	Current study

The calibration curve of the VAG biosensor in Figure 5(d) was obtained by plotting the change in phase against MC-LR concentrations at a frequency of 167 mHz. The change in phase increased linearly (i.e. R^2=0.97) with the logarithm of MC-LR concentration over 5 decades between 0.001 and 10 µg/L. Saturation of response was not observed within the MC-LR concentration range. The biosensor exhibited a sensitivity (or the slope, m) of 0.46° ± 0.06° per decade for MC-LR in PBS performed in triplicate. It is worth noting that the biosensors showed no significant response (0.04 ± 0.006°) to just PBS sample (i.e. without MC-LR as negative sample). Hence, this confirm that the biosensing response was due to the binding of MC-LR at the electrodes. For comparison, biosensing results in Figure S7 obtained from printed graphene biosensors without photonic annealing revealed inconclusive response. The LoD for MC-LR detection was calculated to be 1.2 ng/L using the most common method [55], which is well below 1 µg/L set by the World Health Organization (WHO)[56] and also those obtained previously by others using mainly faradaic EIS based biosensors as shown in Table 1. Two other most common freshwater algal toxin variants (i.e. MC-RR and MC-LW) were selected to assess the biosensor selectivity towards MC-LR detection. As shown in Figure 5(e), detection recovery rate for 0.1 µg/L MC-LR, MC-LW and MC-RR mixture in PBS was 91.8% of the same concentration of MC-LR on its own (i.e. without any interfering variants). These results demonstrated high selectivity of the VAG biosensor functionalized with monoclonal MC-LR antibody. Moreover, long term stability of the biosensors was also examined as shown in Figure 5(e). After one- and three-weeks storage in the freezer, 108.8 % and 99.4 % of initial responses in phase shift were obtained to detect 0.1 µg/L MC-LR in PBS, respectively. A large relative standard deviation (RSD) could be caused by the gradual deterioration and loosening of immobilized antibodies after a long-term storage. The MC-LR detection performance was also validated using tap water samples in Swansea, UK (with total organic carbon of 0.91 mg/L, pH 7.8 and conductivity of 127.89 µs/cm), showing an excellent 98.4% recovery for the detection of 0.1 µg/L MC-LR.

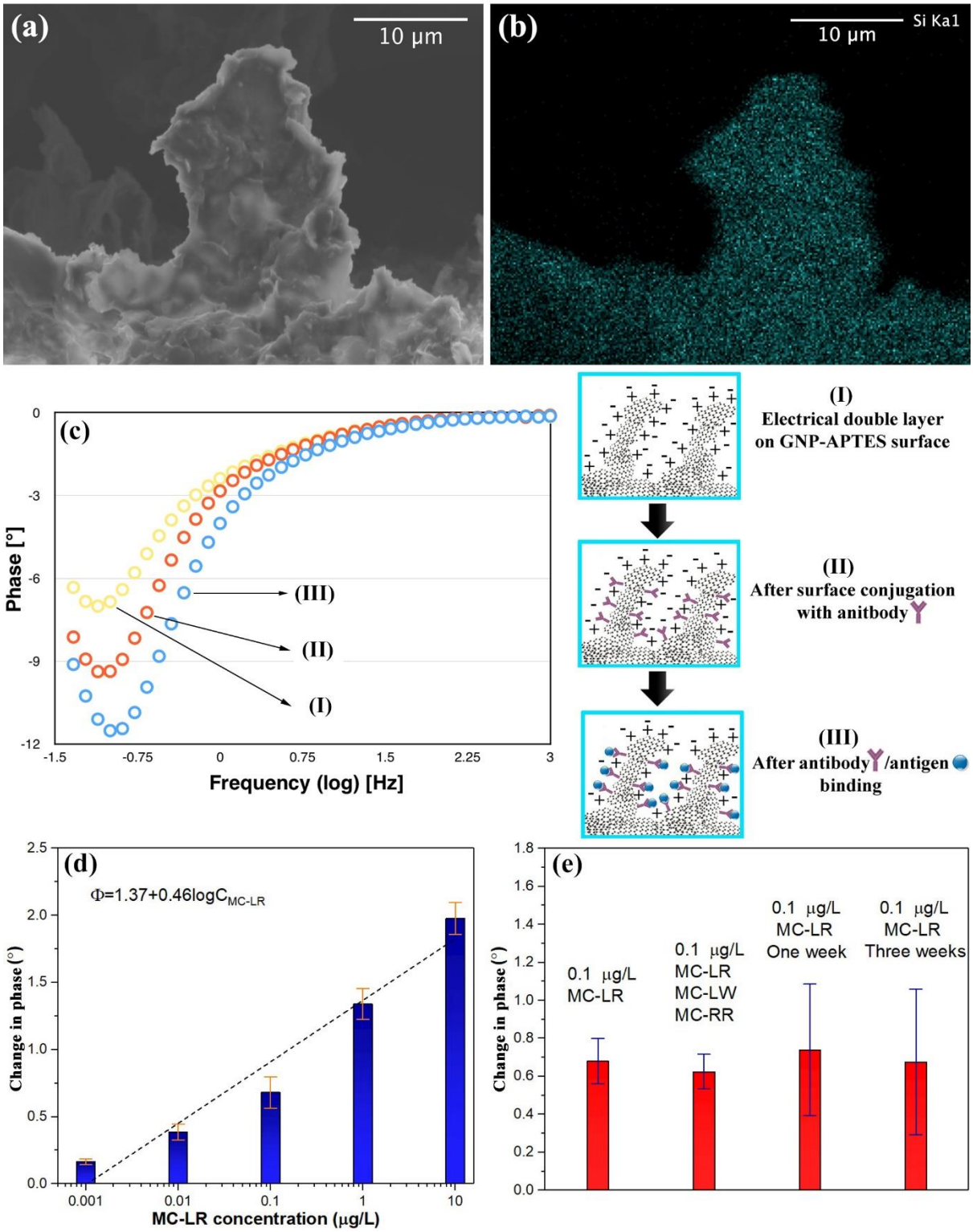

Figure 5 (a) High magnification cross-sectional SEM image and corresponding (b) EDX mapping of silicon on the VAG electrodes; (c) Bode plots from non-faradaic EIS measurements of VAG biosensor after APTES coating, immobilization of antibody and MC-LR conjugation; (d) Change in phase shift, Φ, at VAG biosensors with MC-LR concentrations (C_{MC-LR}) (error bars: SD, n = 3); (e) Selectivity and storability tests of the VAG biosensors (error bars: SD, n = 3).

3. Conclusion

Label-free non-faradaic VAG biosensors have been showcased for the ultra-sensitive detection of algal toxin (i.e. MC-LR) in drinking water supply via non-faradaic EIS technique. The biosensor,

consisting of graphene interdigitated electrodes, was fabricated using roll-to-roll flexographic printing of ball-milled GNP/EC ink and then followed by photonic annealing that partially removed the polymeric binder in the printed graphene. As a result, VAG structures were formed at the electrode surface, which provided maximum specific surface area for ultra-sensitive biosensing application. A spray coating technique was employed to functionalize the biosensor in order to preserve the VAG structures. Prior to immobilization of MC-LR antibodies on the biosensor, a uniform coverage of APTES, which acted as an insulating SAM for non-faradaic EIS biosensors, was spray-coated onto the VAG. The effectiveness of the spray coated APTES was studied using EDX and CV techniques. The change in phase from the non-faradic EIS measurement was obtained at a frequency of 167 mHz. At this frequency, an optimal linear response from the antibody/antigen conjugation was observed at the VAG biosensors, of which the correlation was subsequently established between non-faradaic EIS phase change and logarithm of MC-LR concentration (i.e. 0.001-10 µg/L). An excellent sensitivity of 0.46 degree per decade and LoD of 1.2 ng/L were achieved with great reproducibility, selectivity and stability. Finally, the VAG biosensor was validated using local tap water samples and experienced minimal matrix effects from other factors, such as metal ions, in the water. Such low-cost, easy to use and ultra-sensitive VAG biosensor is ideal for large-scale early screening of contaminations in drinking water and detection of diseases in biomedical applications.

Support Information

The Supporting Information is available free of charge on the ACS Publications website.

Author contributions

[†]L.W. and [†]W.Z. performed the experiments and analysed the data, contributing equally to this work. K.S.T. and W.Z. designed and supervised the research. S.S. and D.D. assisted in flexographic printing and photonic annealing.

Notes

The authors declare that there is no competing financial interest.

Acknowledgement

Dr Wei Zhang would like to acknowledge the financial support from EU Horizon 2020 Marie Skłodowska-Curie Actions Individual Fellowship (No.743993). Authors would also like to thank Dr Yubiao Niu in Advanced Imaging Materials (AIM), Dr Harrison Lee in Materials Research Centre (MRC), Mr Y. C. Lau and Dr Ben Clifford from Welsh Centre for Printing and Coating (WCPC) for their technical support in the characterisation of VAG biosensors.

References

[1] Arco, L. G. D.; Zhang, Y.; Schlenker, C. W.; Ryu, K., Thompson, M. E.; Zhou, C. W. Continuous, Highly Flexible, and Transparent Graphene Films by Chemical Vapor Deposition for Organic Photovoltaics. *ACS Nano* **2010**, *4*, 2865-2873.

[2] Li, H.; Zhang, W.; Zou, L.; Pan, L. K.; Sun Z. Synthesis of TiO_2-graphene Composites via Visible-Light Photocatalytic Reduction of Graphene Oxide. *J. Mater. Res.* **2011**, *26*, 970-973.

[3] Zhang, W.; Jia, B. Toward Anti-fouling Capacitive Deionization by Using Visible-light Reduced TiO_2/graphene Nanocomposites. *MRS Commun.* **2015**, *5*, 613-617.

[4] Bae, S.; Kim, H.; Lee, Y.; Xu, X. F.; Park, J. S.; Zheng, Y.; Balakrishnan, J.; Lei, T.; Kim, H.; Song, Y.; Kim, Y.; Kim, K.; Özyilmaz, B.; Ahn, J.; Hong, B.; Iijima, S. Roll-to-roll Production of 30-inch Graphene Films for Transparent Electrodes. *Nat. Nanotechnol.* **2010**, *5*, 574-578.

[5] Jia, B.; Wang, Q.; Zhang, W.; Lin, B.; Yuan, N.; Ding, J.; Ren, Y.; Chu, F. A New Oil/water Interfacial Assembly of Ultrathin Graphene Films. *RSC Adv.* **2014**, 4, 34566-34571.

[6] Pinto, A. M.; Goncalves, I. C.; Magalhaes, F. D. Graphene-based Materials Biocompatibility: A Review. *Colloids Surf. B* **2013**, *111*, 188-202.

[7] Wang, X.; Jia, B.; Zhang, W.; Lin, B.; Wang, Q.; Ding, J. Developing Modified Graphene Oxide Based Sensor for Lead Ions Detection in Water. *ChemistrySelect*, **2016**, *1*, 1751-1755.
[8] Li, R.; Xia, Q.; Li, Z.; Sun, X.; Liu, J. Electrochemical Immunosensor for Ultrasensitive Detection of Microcystin-LR Based on Graphene-gold Nanocomposite/Functional Conducting Polymer/Gold Nanoparticle/Ionic Liquid Composite Film with Electrodeposition. *Biosens. Bioelectron.* **2013**, *44*, 235-240.
[9] Wei, Q.; Zhao, Y.; Du, B.; Wu, D.; Cai, Y.; Mao, K.; Li, H.; Xu, C. Nanoporous PtRu Alloy Enhancer Nonenzymatic Immunosensor for Ultrasensitive Detection of Microcystin-LR. *Adv. Fun. Mater.* **2011**, *21*, 4193-4198.
[10] Eissa, S.; Ng, A.; Siaj, M.; Zourob, M. Label-free Voltammetric Aptasensor for the Sensitive Detection of Microcystin-LR Using Graphene-modified Electrodes. *Anal. Chem.* **2014**, *86*, 7551-7557.
[11] Zhao, H.; Tian, J.; Quan, X. A Graphene and Multienzyme Functionalized Carbon Nanosphere-based Electrochemical Immunosensor for Microcystin-LR Detection. *Colloids Surf. B* **2013**, *103*, 38-44.
[12] Davami, K.; Shaygan, M.; Kheirabi, N.; Zhao, J.; Kovalenko, D. A.; Rümmeli M. H.; Opitz, J.; Cuniberti, G.; Lee, J.; Meyyappan, M. Synthesis and Characterization of Carbon Nanowalls on Different Substrates by Radio Frequency Plasma Enhanced Chemical Vapor Deposition. *Carbon* **2014**, *72*, 372-380.
[13] Yu, K.; Wang, P.; Lu, G.; Chen, K.; Bo, Z.; Chen, J. Patterning Vertically Oriented Graphene Sheets for Nanodevice Applications. *J. Phys. Chem. Lett.* **2011**, *2*, 537-542.
[14] Lloyd, J.S.; Fung, C.M.; Deganello, D.; Wang, R.J.; Maffeis, T.G.G.; Lau, S.P.; Teng, K.S. Flexographic Printing-assisted Fabrication of ZnO Nanowire Devices. *Nanotechnology* **2013**, *24*, 195602.
[15] Benson, J.; Fung, C. M.; Lloyd, J. S.; Deganello, D.; Smith, N. A.; Teng, K. S. Direct Patterning of Gold Nanoparticles Using Flexographic Printing for Biosensing Applications. *Nanoscale Res. Lett.* **2015**, *10*, 127.
[16] Fung, C.M.; Lloyd, J.S.; Samavat, S.; Deganello, D.; K.S. Teng, K.S. Facile Fabrication of Electrochemical ZnO Nanowire Glucose Biosensor Using Roll to Roll Printing Technique. *Sens. Actuators B Chem.* **2017**, *247*, 807-813.
[17] Assaifan, A. K.; Lloyd, J. S.; Siamak, S.; Deganello, D.; Stanton, R. J.; Teng, K. S. Nanotextured Surface on Flexographic Printed ZnO Thin Films for Low-cost Non-faradaic Biosensors. *ACS Appl. Mater. Interfaces* **2016**, *8*, 33802-33810.
[18] Baker, J.; Deganello, D.; Gethin, D. T.; Watson, T. M. Flexographic Printing of Graphene Nanoplatelet Ink to Replace Platinum as Counter Electrode Catalyst in Flexible Dye Sensitised Solar Cell. *Mater. Res. Innov.* **2014**, *18*, 86–90.
[19] Fischer, T.; Wetzold, N.; Kroll, L.; Hübler, A.; Hu, A. Flexographic Printed Carbon Nanotubes on Polycarbonate Films Yielding High Heating Rates. *J. Appl. Polym. Sci.* **2013**, *129*, 2112–2120.
[20] Paglia, F.; Vak, D.; van Embden, J.; Chesman, A.; Martucci, A.; Jasieniak, J. J.; Gaspera, E. D. Photonic Sintering of Copper Through the Controlled Reduction of Printed CuO Nanocrystals. *ACS Appl. Mater. Interfaces* **2015**, *7*, 25473-25478.
[21] Arapov, K.; Bex, G.; Hendriks, R.; Rubingh, E.; Abbel, R.; With, G.D.; Friedrich, H. Conductivity Enhancement of Binder-based Graphene Inks by Photonic Annealing and Subsequent Compression Rolling. *Adv. Eng. Mater.* **2016**, *18*, 1234-1239.
[22] Secor, E.B.; Gao, T.Z.; Santos, M.H.D.; Wallace, S.G.; Putz, K.W.; Hersam, M.C. Combustion-assisted Photonic Annealing of Printable Graphene Inks via Exothermic Binders. *ACS Appl. Mater. Interfaces* **2017**, *9*, 29418-29423.
[23] Das, S.R.; Nian Q.; Cargill, A.A.; Hondred, J.A.; Ding, S.; Saei, M.; Cheng, G. J.; Claussen, J. C. 3D Nanostructured Inkjet Printed Graphene via UV-pulsed Laser Irradiation Enables Paper-based Electronics and Electrochemical Devices. *Nanoscale* **2016**, *8*, 15870-15879.
[24] Das, S.R.; Srinivasan, S.; Stromberg, L.R.; He, Q.; Garland, N.; Strazheim, W. E.; Ajayan, P.M.; Balasubramanian, G.; Claussen, J. C. Superhydrophobic Inkjet Printed Flexible Graphene Circuits via Direct-pulsed Laser Writing. *Nanoscale* **2017**, *9*, 19058-19065.
[25] Cai, X.; Baldelli, S. Surface Barrier Properties of Self-assembly Monolayers as Deduced by Sum Frequency Generation Spectroscopy and Electrochemistry. *J. Phys. Chem. C* **2011**, *115*, 19178-19189.

[26] Boubour, E.; Bruce Lennox, R. Insulating Properties of Self-assembled Monolayers Monitored by Impedance Spectroscopy. *Langmuir* **2000**, *16*, 4222-4228.
[27] Carmichaeal, W. W. Cyanobacteria Secondary Metabolites-the Cyanotoxins. *J. Appl. Bacteriol.* **1992**, *72*, 445-459.
[28] Zhang, W.; Zhang, Y.; Fan, R.; Lewis, R. A Facile TiO_2/PVDF Composite Membrane Synthesis and Their Application in Water Purification. *J. Nanoparticle Res.* **2016**, *18*, 31.
[29] Zhang, W.; Zou, L.; Wang, L. Visible-light Assisted Methylene Blue (MB) Removal by Novel TiO_2/adsorbent Nanocomposites. *Water Sc. Technol.* **2010**, *61*, 2863-2871.
[30] Zhang, W.; Dixon, M.B.; Saint, C.; Teng, K.S.; Furumai, H. Electrochemical Biosensing of Algal Toxins in Water: The Current State-of-art? *ACS Sens.* **2018**, *3*, 1233-1245.
[31] Zhang, W.; Wang, L.; Yang, Y.; Gaskin, P.; Teng, K.S. Recent Advances on Electrochemical Sensors for the Detection of Organic Disinfection By-products in Water. *ACS Sens.* **2019**, *4*, 1138-1150.
[32] Van Schaftinghen, T.; Le Pen, C.; Terryn, H.; Horzenberger, F. Investigation of the Barrier Properties of Silanes on Cold Rolled Steel. *Electrochim. Acta* **2004**, *49*, 2997−3004.
[33] Lai, W. A.; Lin, C. H.; Yang, Y. S.; Lu, M. S. C. Ultrasensitive and Label-free Detection of Pathogenic Avian Influenza DNA by Using CMOS Impedimetric Sensors. *Biosens. Bioelectron.* 2012, 35, 456−460.
[34] Wilson, N.R.; Pandey, P.A.; Beanland, R.; Young, R. J.; Kinloch, I.A.; Gong, L.; Liu, Z.; Suenaga, K.; Rourke, J. P.; York, S. J.; Sloan, J. Graphene Oxide: Structural Analysis and Application as a Highly Transparent Support for Electron Microscopy. *ACS Nano* **2009**, *3*, 2547.
[35] Ferrari, A.C.; Robertson, J. Interpretation of Raman Spectra of Disordered and Amorphous Carbon. *Phys. Rev. B* **2000**, *61*, 14095.
[36] Saito, R.; Hofmann, M.; Dresselhaus, G.; Jorio, A.; Dresselhaus, M. S. Raman Spectroscopy of Graphene and Carbon Nanotubes. *Adv. Phys.* **2011**, *60*, 413-550.
[37] Tuinstra, F.; Koenig, J.L. Raman Spectrum of Graphite. *J. Chem. Phys.* **1970**, *53*(3), 1126-1130.
[38] Saito, R.; Jorio, A.; Souza Filho, A. G.; Dresselhaus, G.; Dresselhaus, M. S.; Pimenta, M. A. Probing Phonon Dispersion Relations of Graphite by Double Resonance Raman Scattering. *Phys. Rev. Lett.* **2001**, *88*, 027401.
[39] Childres, I.; Jauregui, L. A.; Tian, J.; Chen, Y. P. Effect of Oxygen Plasma Etching on Graphene Studied Using Raman Spectroscopy and Electronic Transport Measurements. *New J. Phys.* **2011**, *13*, 025008.
[40] Lee, C.M.; Kubicki, J.D.; Fan, B.; Zhong, L.; Jarvis, M.C.; Kim, S.H. Hydrogen-bonding Network and OH Stretch Vibration of Cellulose: Comparison of Computational Modeling with Polarized IR and SFG Spectra. *J. Phys. Chem. B* **2015**, *119*, 15138-15149.
[41] Guadagno, L.; Vertuccio, L.; Naddeo, C.; Calabrese, E.; Barra, G.; Raimondo, M.; Sorrentino, A.; Binder, W. H.; Michael, P.; Rana, S. Reversible Self-Healing Carbon-Based Nanocomposites for Structural Applications. *Polymers* **2019**, *11*, 903.
[42] Graf, D.; Molitor, F.; Ensslin, K.; Stampfer, C.; Jungen, A.; Hierold, C.; Wirtz, L. Spatially Resolved Raman Spectroscopy of Single- and Few-Layer Graphene. *Nano Lett.* **2007**, *7*, 238-242.
[43] Hao, Y.; Wang, Y.; Wang, L.; Ni, Z.; Wang, Z.; Wang, R.; Koo, C.K.; Shen, Z.; Thong, J.T.L. Probing Layer Number and Stacking Order of Few-layer Graphene by Raman Spectroscopy. *Small*, **2010**, *6*, 195-200.
[44] Zhang, W.; Jia, B.; Furumai, H. Fabrication of Graphene Film Composite Electrochemical Biosensor as a Pre-screening Algal Toxin Detection Tool in the Event of Water Contamination. *Sci. Rep.* **2018**, *8*, 10686.
[45] Ravani, F.; Papagelis, K.; Dracopoulos, V.; Parthenios, J.; Dassios, K. G.; Siokou, A.; Galiotis, C. Graphene Production by Dissociation of Camphor Molecules on Nickel Substrate. *Thin Solid Films*, **2013**, *527*, 31-37.
[46] Arapov, K.; Rubingh, E.; Abbel, R.; Laven, J.; de With, G.; Friedrich, H. Conductive Screen Printing Inks by Gelation of Graphene Dispersions. *Adv. Funct. Mater.* **2016**, *26*(4), 586-593.
[47] Arranz, A.; Palacio, C.; García-Fresnadillo, D.; Orellana, G.; Navarro, A.; Muñoz, E. Influence of Surface Hydroxylation on 3-aminopropyltriethoxysilane Growth Mode during Chemical Functionalization of GaN Surfaces: An Angle-resolved X-ray Photoelectron Spectroscopy Study. *Langmuir* **2008**, *24*, 8667-8671.

[48] Janek, R.; Fawcett, W.; Ulman, A. Impedance Spectroscopy of Self-assembled Monolayers on Au (111): Sodium Ferrocyanide Charge Transfer at Modified Electrodes. *Langmuir* **1998**, *14*, 3011-3018.
[49] Daniels, J. S.; Pourmand, N. Label-free Impedance Biosensors: Opportunities and Challenges. *Electroanalysis* 2007, *19*, 1239−1257.
[50] Zaccari, I.; Catchpole, B.G.; Laurenson, S. X.; Davies, A.G.; Wälti, C. Improving the Dielectric Properties of Ethylene-glycol Alkanethiol Self-assembled Monolayers. *Langmuir* **2014**, *30*, 1321-1326.
[51] Boubour, E.; Lennox, R. Potential-induced Defects in n-alkanethiol Self- assembled Monolayers Monitored by Impedance Spectroscopy. *J. Phys. Chem. B* **2000**, *104*, 9004–9010.
[52] Han, C.; Doepke, A.; Cho, W.; Likodimos, V.; de la Cruz, A. A.; Back, T.; Heineman, W. R.; Halsall, H. B.; Shanov, V. N.; Schulz, M. J.; Falaras, P.; Dionysiou, D. D. A Multiwalled-carbon-nanotube-based Biosensor for Monitoring Microcystin-LR in Sources of Drinking Water Supplies. *Adv. Funct. Mater.* **2013**, *23*, 1807–1816.
[53] Zhang, W.; Han, C.; Jia, B.; Saint, C.; Nadagouda, M.; Falaras, P.; Sygellou, L.; Vogiazi, V.; Dionysiou, D.D. A 3D Graphene-based Biosensor as an Early Microcystin-LR Screening Tool in Sources of Drinking Water Supply. *Electrochim. Acta* **2017**, *236*, 319-327.
[54] Hou, L.; Ding, Y.; Zhang, L.; Guo, Y.; Li, M.; Chen, Z.; Wu, X. An Ultrasensitive Competitive Immunosensor for Impedimetric Detection of Microcystin-LR via Antibody-conjugated Enzymatic Biocatalytic Precipitation. *Sens. Actuators B Chem.* **2016**, *233*, 63-70.
[55] Fassel, V. A. Nomenclature, Symbols, Units and Their Usage in Spectrochemical Analysis—II. Data Interpretation Analytical Chemistry Division. *Spectrochim. Acta B At. Spectrosc.* **1978**, *33*, 241–245.
[56] World Health Organization, Guidelines for Drinking-Water Quality, 2nd ed. Addendum to Vol. 1. Recommendations, Geneva, World Health Organization **1998**, p. 13.

For TOC Only

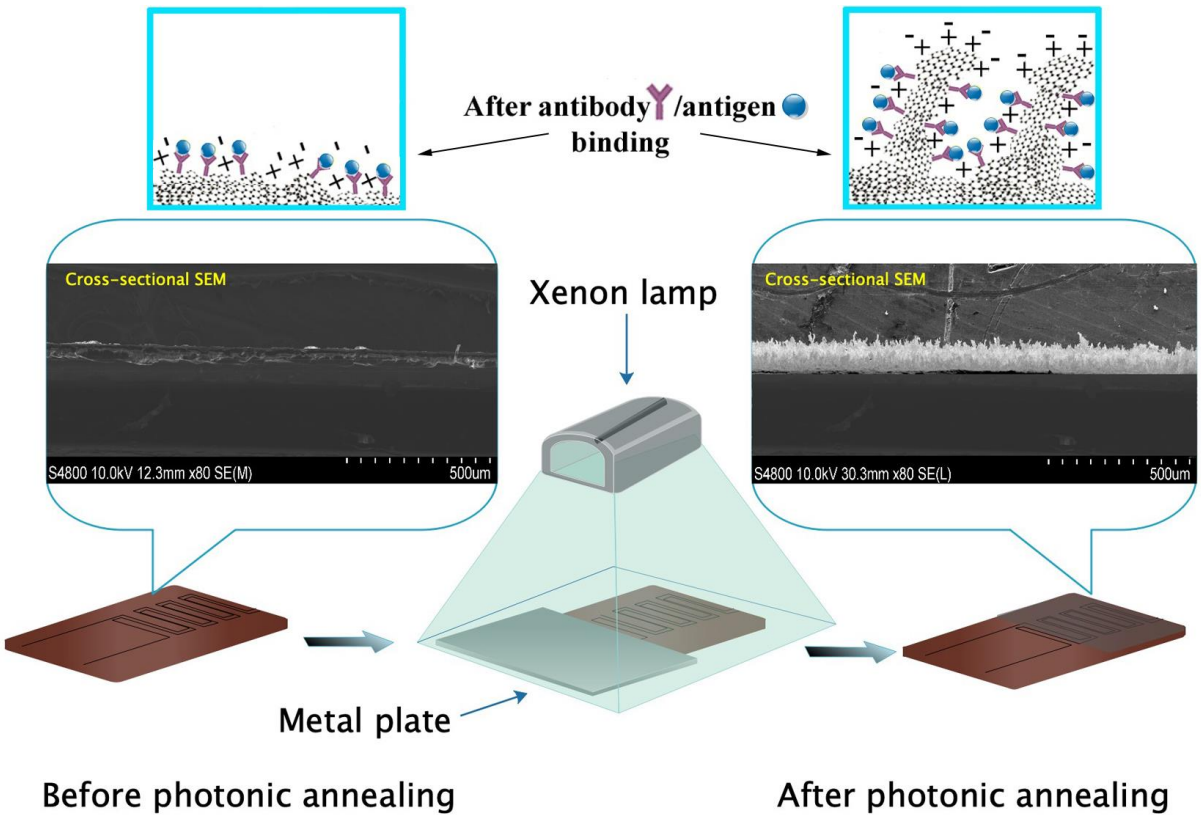
After antibody /antigen binding
Cross-sectional SEM
S4800 10.0kV 12.3mm x80 SE(M)
500um
Xenon lamp
Cross-sectional SEM
S4800 10.0kV 30.3mm x80 SE(L)
500um
Metal plate
Before photonic annealing
After photonic annealing